Cross density of states and mode connectivity: Probing wave localization in complex media

Antoine Canaguier-Durand,[1] Romain Pierrat,[2] and Rémi Carminati[2,*]
[1]*Laboratoire Kastler Brossel, Sorbonne Université, CNRS, ENS-PSL University, Collège de France, Paris, France*
[2]*ESPCI Paris, PSL University, CNRS, Institut Langevin, 1 rue Jussieu, F-75005, Paris, France*

(Received 10 July 2018; published 22 January 2019)

We introduce the mode connectivity as a measure of the number of eigenmodes of a wave equation connecting two points at a given frequency. Based on numerical simulations of scattering of electromagnetic waves in disordered media, we show that the connectivity discriminates between the diffusive and the Anderson localized regimes. For practical measurements, the connectivity is encoded in the second-order coherence function characterizing the intensity emitted by two incoherent classical or quantum dipole sources. The analysis applies to all processes in which spatially localized modes build up, and to all kinds of waves.

DOI: 10.1103/PhysRevA.99.013835

I. INTRODUCTION

Spatially localized modes are key elements in the description of many phenomena in mesoscopic and wave physics [1], and their control is a central issue in photonics, acoustics, or microwave engineering. Indeed, wave transport through disordered media is substantially affected by Anderson localization [2]. Surface-plasmon modes on percolated metallic films also undergo a localization process in certain conditions, producing a subwavelength concentration of energy of interest in nanophotonics [3]. In photonics and acoustics (phononics), band gaps in periodic structures [4,5] and cavity modes are used to enhance wave-matter interaction, e.g., to enter the regimes of cavity quantum electrodynamics (QED) [6] or optomechanics [7,8]. An underlying question in the description of localization phenomena, and in the design of artificial structures producing localized modes, is the characterization of an isolated mode (e.g., as a signature of Anderson localization itself, or to reach cavity QED regimes [9,10]), and the measure of the spatial connection between individual modes (e.g., in the description of transport through a chain of weakly connected modes [11]).

In this article, we introduce the concept of mode connectivity, defined from the local and cross densities of states (LDOS and CDOS), as a measure of the connection between two points sustained by the eigenmodes at a given frequency. We focus on electromagnetic waves, but the concept applies to other kinds of waves. As an illustration, we show that the mode connectivity allows one to discriminate between diffusive transport and Anderson localization in disordered media. We then define observables that depend directly on the connectivity and the LDOS, and that could be measured from the power emitted by two dipole sources placed inside the medium or at close proximity to its surface. We examine separately the case of classical sources (antennas) and of quantum emitters (single-photon sources). The proposed approach could provide an unambiguous probe of Anderson localization of electromagnetic waves in 3D, whose existence remains a debated issue [12].

II. CROSS DENSITY OF STATES AND CONNECTIVITY

For a monochromatic electromagnetic field at a frequency ω, we define the CDOS ρ_{12} as [13]

$$\rho_{12} = \frac{2\omega}{\pi c^2}\mathrm{Im}[\mathbf{u}_1 \cdot \mathbf{G}(\mathbf{r}_1, \mathbf{r}_2, \omega)\mathbf{u}_2], \tag{1}$$

where $\mathbf{r}_1$ and $\mathbf{r}_2$ are two points, $\mathbf{u}_1$ and $\mathbf{u}_2$ are two unit vectors, and c is the speed of light in vacuum. In this expression, $\mathbf{G}(\mathbf{r}_1, \mathbf{r}_2, \omega)$ is the electric Green function that connects an electric-dipole source $\mathbf{p}$ at point $\mathbf{r}_2$ to the electric field generated at point $\mathbf{r}_1$ through the relation $\mathbf{E}(\mathbf{r}_1) = \mu_0\,\omega^2\,\mathbf{G}(\mathbf{r}_1, \mathbf{r}_2, \omega)\mathbf{p}$. Note that we consider here a partial CDOS, projected over two polarization directions $\mathbf{u}_1$ and $\mathbf{u}_2$, that differs from the full CDOS initially introduced in Ref. [13] in which the polarization degrees of freedom are averaged out.

The CDOS measures the connection between point $\mathbf{r}_1$ and $\mathbf{r}_2$ sustained by the eigenmodes [13,14]. Interestingly, the CDOS obeys the inequality

$$\rho_{12} \leqslant \sqrt{\rho_{11}\rho_{22}}, \tag{2}$$

where $\rho_{ii} = 2\omega/(\pi c^2)\mathrm{Im}[\mathbf{u}_i \cdot \mathbf{G}(\mathbf{r}_i, \mathbf{r}_i, \omega)\mathbf{u}_i]$ is the (partial) LDOS that measures the weighted contribution of eigenmodes at position $\mathbf{r}_i$, projected along the polarization direction $\mathbf{u}_i$ [15]. The inequality (2) was initially derived in Ref. [16], and the proof is recalled in Appendix A, for consistency. This naturally leads to the introduction of the mode connectivity

$$\mathcal{C}_{12} = \frac{|\rho_{12}|}{\sqrt{\rho_{11}\rho_{22}}}, \tag{3}$$

a dimensionless number lying within [0,1]. The two observation points $\mathbf{r}_1$ and $\mathbf{r}_2$ are highly connected at frequency ω when $\mathcal{C}_{12} \simeq 1$, and weakly connected when $\mathcal{C}_{12} \simeq 0$.

A particular case of a strong connection between two points is the single-mode regime, for which the equality $\mathcal{C}_{12} = 1$ is satisfied, as we shall now see. In a single-mode

*remi.carminati@espci.fr

lossless cavity, the electric Green function can be expanded in the form

$$\mathbf{G}(\mathbf{r}_1,\mathbf{r}_2,\omega) = c^2\,\mathbf{e}_M(\mathbf{r}_1)\mathbf{e}_M^*(\mathbf{r}_2)\left[\mathrm{P}\left(\frac{1}{\omega_M^2-\omega^2}\right) + \frac{i\pi}{2\omega_n}\delta(\omega-\omega_M)\right], \tag{4}$$

where $\mathbf{e}_M(\mathbf{r})$ is the eigenmode and ω_M the eigenfrequency of the vector Helmholtz equation (see, for example, Ref. [15]). Note that we use a tensor notation such that $[\mathbf{e}_M(\mathbf{r}_1)\mathbf{e}_M^*(\mathbf{r}_2)]\mathbf{v} = [\mathbf{e}_M^*(\mathbf{r}_2)\cdot\mathbf{v}]\mathbf{e}_M(\mathbf{r}_1)$ for any vector $\mathbf{v}$. In the presence of weak losses (by absorption or radiation), we can write

$$\mathbf{G}(\mathbf{r}_1,\mathbf{r}_2,\omega) = c^2\,\frac{\mathbf{e}_M(\mathbf{r}_1)\mathbf{e}_M^*(\mathbf{r}_2)}{\omega_M^2-\omega^2-i\omega\gamma_M}, \tag{5}$$

where γ_M is the mode damping rate. This phenomenological expression is built in such a way as to recover Eq. (4) in the limit $\gamma_M \to 0$, and is only valid for a large quality factor $Q = \omega_M/\gamma_M$, and for near-resonant frequencies. A more general approach could be built using quasinormal modes [14], but we assume here that the conditions of the phenomenological approach (large Q regime) are satisfied. Using the reciprocity theorem $\mathbf{G}(\mathbf{r}_1,\mathbf{r}_2,\omega) = \mathbf{G}^T(\mathbf{r}_2,\mathbf{r}_1,\omega)$ satisfied by the Green function, one easily shows that $\mathrm{Im}[\mathbf{e}_M(\mathbf{r}_1)\mathbf{e}_M^*(\mathbf{r}_2)] = 0$. As a consequence, the projected CDOS $\rho_{12} = (2\omega/\pi c^2)\mathrm{Im}[\mathbf{u}_1\cdot\mathbf{G}(\mathbf{r}_1,\mathbf{r}_2,\omega)\cdot\mathbf{u}_2]$, with $\mathbf{u}_1$ and $\mathbf{u}_2$ two real unit vectors, reduces to

$$\rho_{12} = \frac{\gamma_M}{2\pi}\,\frac{\mathbf{u}_1\cdot[\mathbf{e}_M(\mathbf{r}_1)\mathbf{e}_M^*(\mathbf{r}_2)]\mathbf{u}_2}{(\omega_M-\omega)^2+\gamma_M^2/4}, \tag{6}$$

where we have used $\omega \simeq \omega_M$ except in the resonant term. Using the definition of the tensor product, this expression can be transformed into

$$\rho_{12} = \frac{\gamma_M}{2\pi}\,\frac{[\mathbf{e}_M^*(\mathbf{r}_2)\cdot\mathbf{u}_2][\mathbf{e}_M(\mathbf{r}_1)\cdot\mathbf{u}_1]}{(\omega_M-\omega)^2+\gamma_M^2/4}. \tag{7}$$

Introducing the LDOS at positions $\mathbf{r}_1$ and $\mathbf{r}_2$,

$$\rho_{11} = \frac{\gamma_M}{2\pi}\,\frac{|\mathbf{u}_1\cdot\mathbf{e}_M(\mathbf{r}_1)|^2}{(\omega_M-\omega)^2+\gamma_M^2/4}, \tag{8}$$

$$\rho_{22} = \frac{\gamma_M}{2\pi}\,\frac{|\mathbf{u}_2\cdot\mathbf{e}_M(\mathbf{r}_2)|^2}{(\omega_M-\omega)^2+\gamma_M^2/4}, \tag{9}$$

one immediately obtains

$$\rho_{12}^2 = \rho_{11}\rho_{22} \tag{10}$$

in the case of a single mode. Note that we have identified the square and the square modulus of the real-valued denominator in ρ_{12}. From the definition of the connectivity [Eq. (3)], we directly see that $\mathcal{C}_{12} = 1$ when the two points $\mathbf{r}_1$ and $\mathbf{r}_2$ are connected by a single weakly dissipative mode.

III. CONNECTIVITY AND ANDERSON LOCALIZATION

Using the connectivity as a measure of the mode connection between two points is of interest, for example, to probe the existence of a single-mode regime, resulting from a specific design of a structure, or from a self-built localization process. As an important application of the concept, we shall now show that the connectivity discriminates between diffusive transport and Anderson localization in disordered media. Identifying an unambiguous marker of these two regimes remains a challenging issue, in particular for electromagnetic waves.

Before analyzing the relevance of the connectivity in this context, we give a qualitative picture of the difference between diffusion and localization in terms of eigenmodes. In the diffusive regime, the eigenmodes overlap both in frequency and space. At a given frequency, the eigenmodes are spatially extended, and any point in the medium is covered by a large number of modes. Conversely, in the localized regime, at a given point and for a given frequency, no more than one mode has a non-negligible contribution [10].

To support this qualitative picture, we provide numerical simulations of scattering of electromagnetic waves in two dimensions (2D). We restrict the simulations to 2D since the existence of Anderson localization of electromagnetic waves in three dimensions (3D) remains an open question, while its existence in 2D has been proven [17,18]. Although the method proposed in this work could provide an unambiguous signature of localization even in 3D, our purpose here is to prove the principle using numerical simulations in a 2D geometry for which the diffusive and localized regimes can be clearly identified. Indeed, even the numerical proof of Anderson localization of electromagnetic waves in 3D remains a matter of debate [12], and we do not intend to solve this issue here.

For the numerical simulations, we consider a medium composed of randomly distributed nonabsorbing subwavelength scatterers. For illustrative purposes we consider TE polarized waves, with the electric field and the two polarization directions $\mathbf{u}_1$ and $\mathbf{u}_2$ perpendicular to the plane containing the scatterers. The scatterers are characterized by their electric polarizability $\alpha(\omega) = (2\Gamma/k_0^2)(\omega_0-\omega-i\Gamma/2)^{-1}$ with resonance frequency $\omega_0 = 3\times10^{15}$ s^{-1}, natural linewidth $\Gamma = 5\times10^{16}$ s^{-1}, and $k_0 = \omega/c = 2\pi/\lambda$, where λ is the wavelength in vacuum. This form of the polarizability is valid for near-resonance frequencies and satisfies energy conservation (or equivalently the optical theorem). The surface density of scatterers is $\rho = 3.98\times10^{12}$ m^{-2}, which corresponds to $N = 2292$ point scatterers located in a square domain with size $L = 24$ μm [see Fig. 1(a)]. From these parameters one can determine the scattering mean free path $\ell_s = (\rho\sigma_s)^{-1}$, and estimate the localization length $\xi = \ell_s\exp(\pi k_0\ell_s/2)$. For $\lambda = 400$ nm, we get $\xi = 4.16\times10^{10}\mu$m $\gg L$ and the medium is in the diffusive regime, while for $\lambda = 1500$ nm, $\xi = 1.5$ μm $\ll L$ and the medium is in the localized regime. The wavelength $\lambda = 1000$ nm provides an intermediate case for which $\xi = 19.6$ μm $\sim L$.

We compute the field in the medium upon illumination by a single dipole source using the coupled dipole method that has been described in previous studies [10]. From the field, one can deduce the Green function and the CDOS or the LDOS based on Eq. (1). Maps of the LDOS inside the medium are displayed in Figs. 1(b)–1(d). In order to avoid border effects and consider only bulk properties, we remove from the maps a 2 μm border [see Fig. 1(a)] that is larger than both $\ell_s = 993$ nm in the diffusive regime ($\lambda = 400$ nm) and $\xi = 1.5$ μm in the localized regime ($\lambda = 1500$ nm). We clearly see that

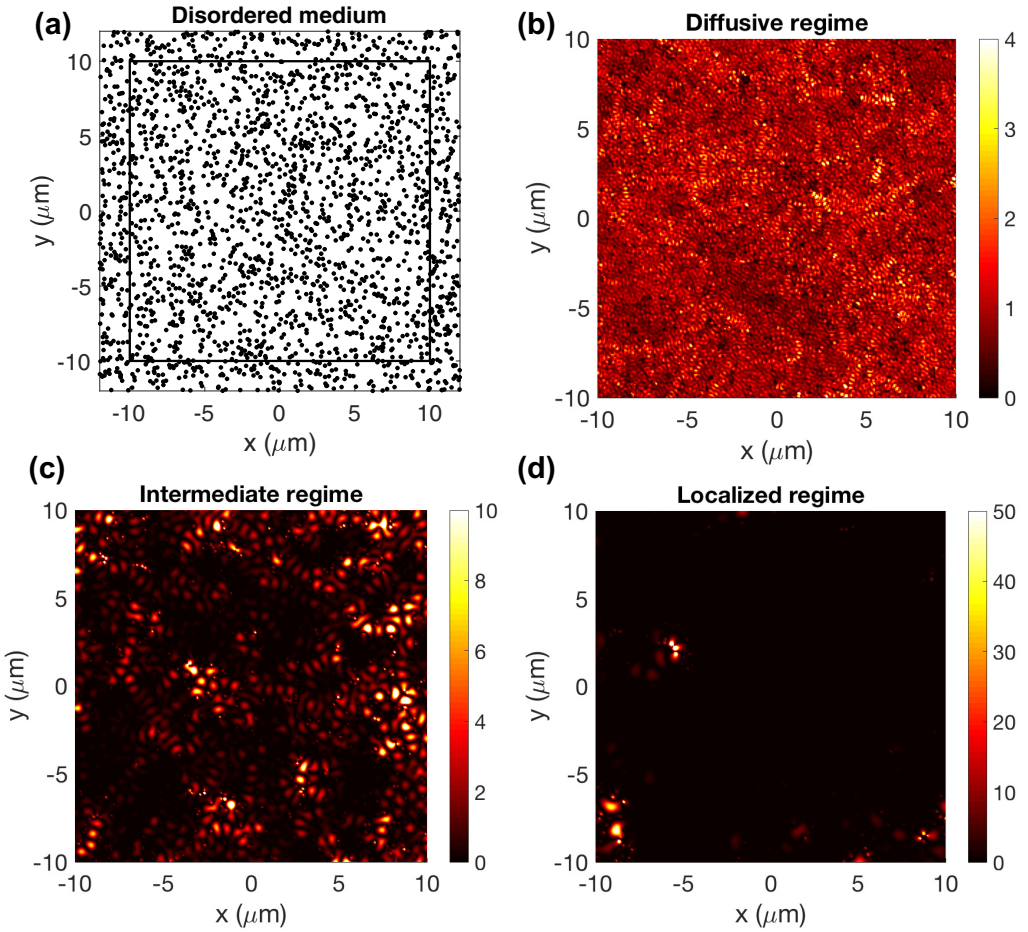

FIG. 1. (a) Realization of a 2D disordered medium with $N = 2292$ subwavelength scatterers. To avoid border effects, fields are calculated within the inner 20 μm by 20 μm square box defined by the solid line. (b)–(d) Calculated LDOS maps. (b) Diffusive regime ($\lambda = 400$ nm). (c) Intermediate regime ($\lambda = 1000$ nm). (d) Localized regime ($\lambda = 1500$ nm).

in the diffusive regime [Fig. 1(b)] the medium supports a spatially homogeneous distribution of LDOS, while in the localized regime [Fig. 1(d)] LDOS spots corresponding to localized modes are clearly visible, whereas a large part of the sample is not covered by any eigenmode.

In free space, for TE polarized waves in 2D, the connectivity for two points separated by a distance $r = |\mathbf{r}_1 - \mathbf{r}_2|$ is simply $\mathcal{C}_0 = |J_0(k_0 r)|$. In this simple case, $\mathcal{C}_0 \simeq 1$ for positions separated by a subwavelength distance ($k_0 r \ll 1$), while two positions far apart ($k_0 r \gg 1$) are poorly connected. From the qualitative behavior described above, we can expect the connectivity $\mathcal{C}_{12}$ to change substantially when the transport regime shifts from diffusive to localized. In the first case we await the connectivity to quickly decrease with distance as in the vacuum case, due to the overlap of numerous eigenmodes. On the opposite, in the localized regime where the modes are spatially separated, the connectivity is expected to fluctuate between $\mathcal{C}_{12} \simeq 1$ (for two points in the same localized mode) and $\mathcal{C}_{12} \simeq 0$ (for unconnected points), the latter being more likely for distance $|\mathbf{r}_1 - \mathbf{r}_2| > \xi$. We have checked this behavior numerically by computing maps of $\mathcal{C}_{12}$ versus $\mathbf{r}_2$, with $\mathbf{r}_1$ fixed at the center of the medium.

The results are shown in Fig. 2, with connectivity maps in the left column and cross sections along the line $y = 0$ in the right column. The top row corresponds to the diffusive regime ($\lambda = 400$ nm), the middle row to the intermediate regime ($\lambda = 1000$ nm), and the bottom row to the localized regime ($\lambda = 1500$ nm). The three maps exhibit large qualitative differences: values of $\mathcal{C}_{12}$ clearly below one are obtained in the diffusive regime (top) except close to the origin, which corroborates the idea that any point in the medium is covered by a large amount of modes. Conversely, in the localized regime (bottom) we observe that the relative connectivity saturates to its maximum ($\mathcal{C}_{12} = 1$) over distances $|\mathbf{r}_1 - \mathbf{r}_2| \sim \xi$. This shows that the relative connectivity is a good marker of the difference between the diffusive and the localized regimes, even in a single realization of the disordered medium. This behavior has been systematically observed for many different realizations and results in different profiles for the ensemble-averaged connectivity (see Appendix C).

IV. FRAMEWORK FOR PRACTICAL IMPLEMENTATION

In this section, we shall discuss the relationship between the connectivity and observables in order to provide a framework for practical implementations. Inspired by previous studies [16,19], a strategy relies on placing two incoherent dipole sources inside the medium (or close to its surface),

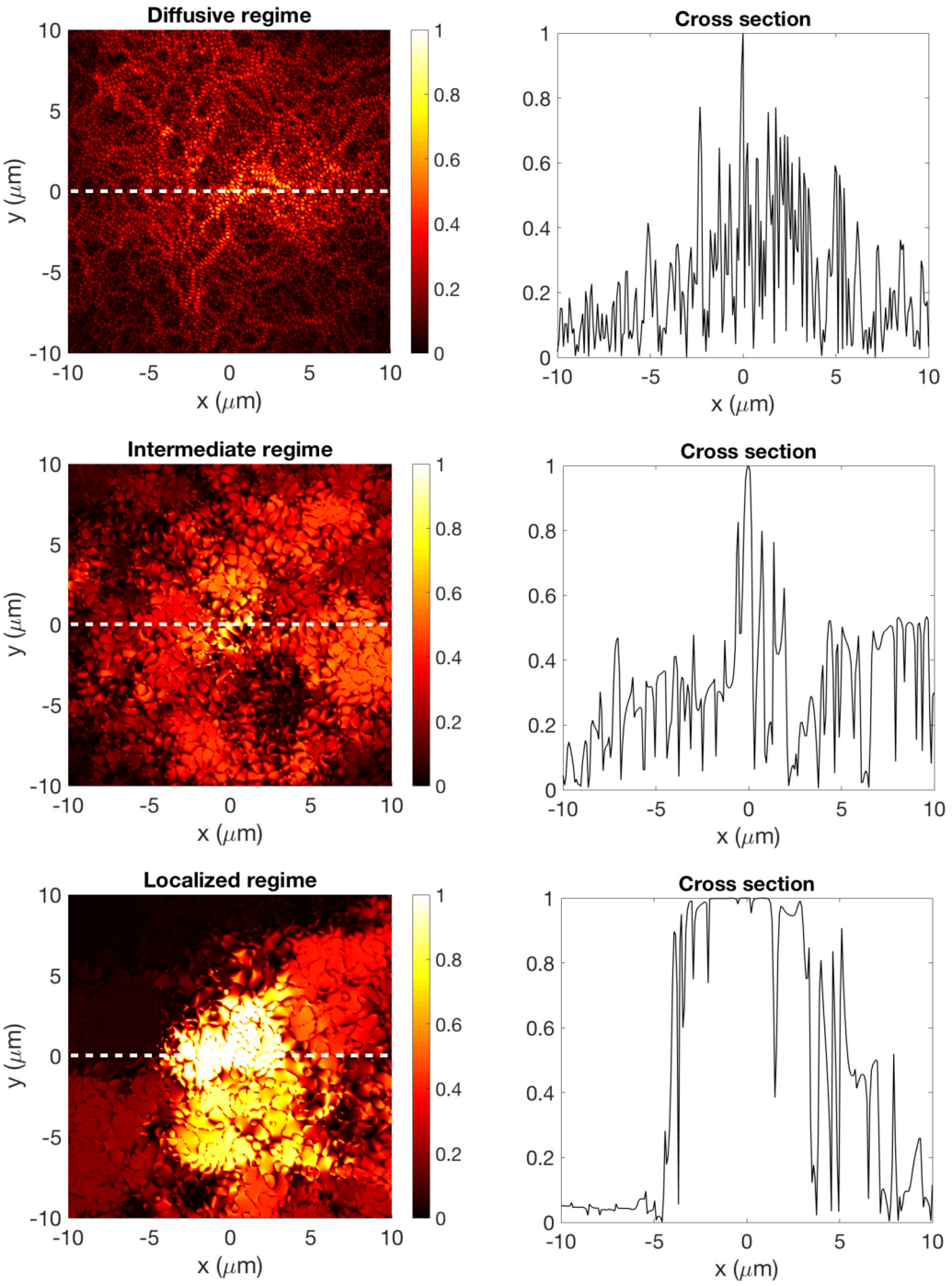

FIG. 2. Left column: maps of the relative connectivity $\mathcal{C}_{12}$ versus $\mathbf{r}_2$, for a fixed position of $\mathbf{r}_1$ (chosen at the center), in a single realization of disorder. Right column: cross sections along the line $y = 0$. From top to bottom the system transits from the diffusive to the localized regimes, with the wavelength as a control parameter.

and measuring the time fluctuations in the total power emitted outside the medium. This strategy is studied here in the general case that covers 2D and 3D geometries. We also consider both classical emitters (e.g., two dipole antennas excited with mutually uncorrelated time-fluctuating currents) and quantum single-photon sources, thus providing tools for a practical implementation in different spectral ranges.

For classical emitters, fluctuations of the total emitted power are characterized by the second-order quantity $G^{(2)}_{\text{class}} = \overline{P^2}/(\overline{P})^2$, where P is the total power emitted by two dipole sources and $\overline{X}$ denotes the time average of X over the temporal fluctuations of the sources. For uncorrelated (incoherent) and similar sources, one shows that [19]

$$G^{(2)}_{\text{class}}(\mathbf{r}_1, \mathbf{r}_2, \omega) = 1 + \tfrac{1}{2}\big(1 - \mathcal{F}^2_{12}\big)\mathcal{C}^2_{12}, \qquad (11)$$

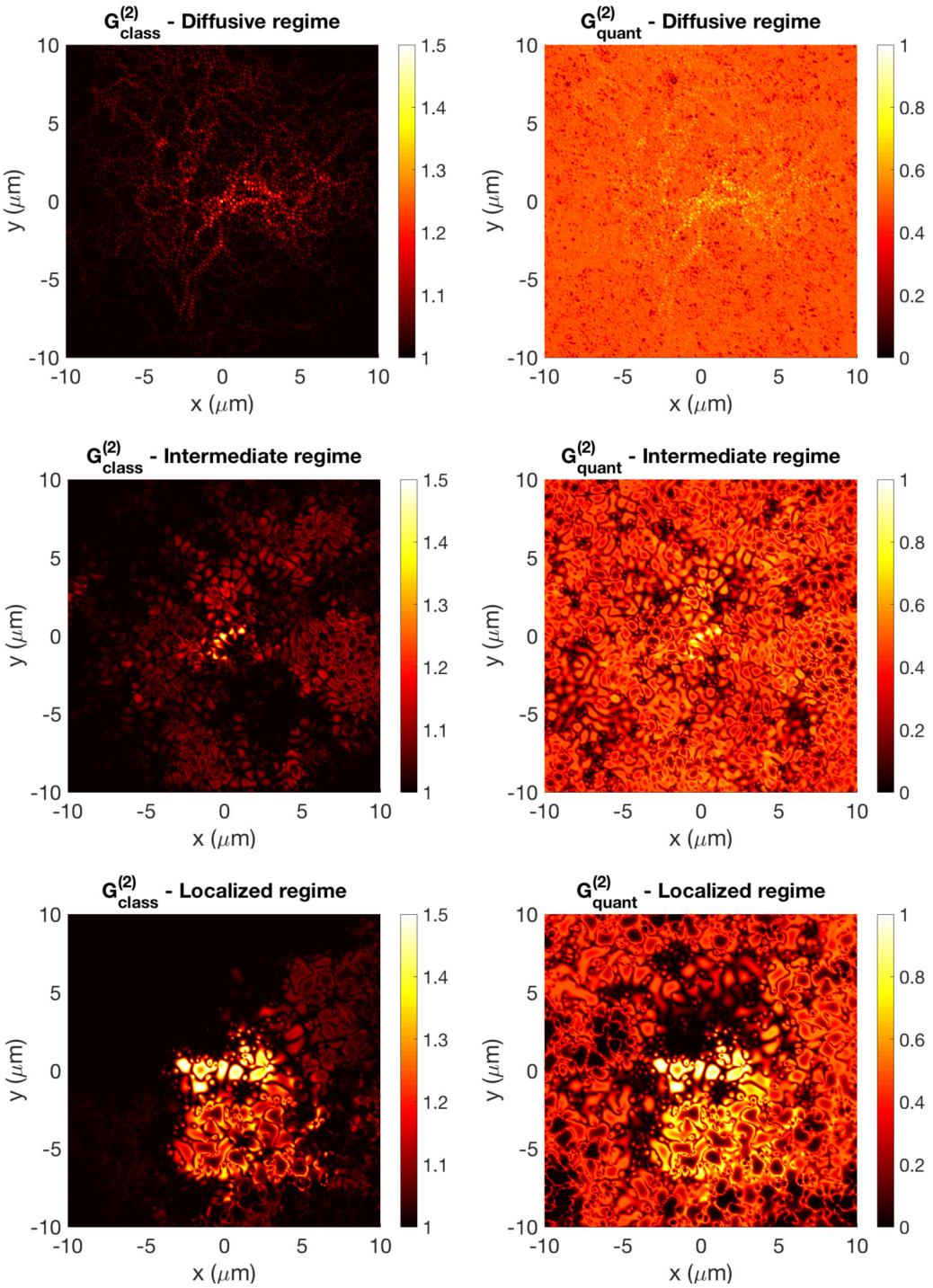

FIG. 3. Maps of the second-order coherence function $G^{(2)}_{\text{class/quant}}(\mathbf{r}_1, \mathbf{r}_2, \omega)$ in a single realization of disorder, with $\mathbf{r}_1$ fixed at the center and $\mathbf{r}_2$ scanning the medium, with classical sources (left) and quantum sources (right).

where $\mathcal{F}_{12}$ is the LDOS contrast defined as

$$\mathcal{F}_{12} = \frac{|\rho_{11} - \rho_{22}|}{\rho_{11} + \rho_{22}}. \tag{12}$$

Although this result can be directly deduced from the analysis in Ref. [19], it is derived in Appendix B for the sake of consistency. The dimensionless quantity $\mathcal{F}_{12}$, that also lies within [0,1], measures the relative difference between the LDOS at positions $\mathbf{r}_1$ and $\mathbf{r}_2$. Values $\mathcal{F}_{12} \simeq 0$ correspond to $\rho_{11} \sim \rho_{22}$, while $\mathcal{F}_{12} \simeq 1$ when $\rho_{11} \ll \rho_{22}$ or $\rho_{11} \gg \rho_{22}$. From Eq. (11), one readily sees that the classical second-order function $G^{(2)}_{\text{class}}$ lies in $[1, 3/2]$ since both $(1 - \mathcal{F}^2_{12})$ and $\mathcal{C}^2_{12}$ are in [0,1].

For two single-photon quantum emitters, the second-order coherence function for measurements integrated over all output channels is defined as $G^{(2)}_{\text{quant}} = \langle P_2 \rangle / \langle P_1 \rangle^2$, where P_1 and P_2 are the single and double photodetection operators integrated over all output channels and the

brackets denote quantum expectation values. Denoting by $\mathbf{\Phi}_1(\mathbf{r}_1,\alpha_1)$ $[\mathbf{\Phi}_2(\mathbf{r}_1,\alpha_1,\mathbf{r}_2,\alpha_2)]$ the single (double) photodetection quantum operators, $\mathbf{r}_1$ and $\mathbf{r}_2$ denoting two detector positions and α_1 and α_2 being two polarization states, one has $P_1 = (\varepsilon_0 c/2)\int_{S_1} d\mathbf{r}_1 \sum_{\alpha_1} \mathbf{\Phi}_1(\mathbf{r}_1,\alpha_1)$ and $P_2 = (\varepsilon_0 c/2)^2 \int_{S_1} d\mathbf{r}_1 \int_{S_2} d\mathbf{r}_2 \sum_{\alpha_1,\alpha_2} \mathbf{\Phi}_2(\mathbf{r}_1,\alpha_1,\mathbf{r}_2,\alpha_2)$. The summation over polarization and the integration over two surfaces S_1 and S_2 enclosing the medium define photodetection processes integrated over all output channels [16]. In the case of two similar emitters initially in the excited state, the second-order coherence function $G^{(2)}_{\text{quant}}$ can be expressed in terms of the LDOS contrast and the relative connectivity in the form

$$G^{(2)}_{\text{quant}}(\mathbf{r}_1,\mathbf{r}_2,\omega) = \tfrac{1}{2}\big(1-\mathcal{F}_{12}^2\big)\big(1+\mathcal{C}_{12}^2\big). \tag{13}$$

This result is directly deduced from the analysis in Ref. [16], and is also derived in Appendix B for consistency. Expression (13) shows that $0 \leqslant G^{(2)}_{\text{quant}} \leqslant 1$, meaning an antibunching behavior in the emission from the two quantum sources.

For both classical or quantum sources, we conclude that second-order coherence functions $G^{(2)}$ are fully determined by the mode connectivity $\mathcal{C}_{12}$ and the LDOS contrast $\mathcal{F}_{12}$. From the maps of the LDOS presented in Fig. 1, we expect $\mathcal{F}_{12}$ to increase when the system goes from the diffusive regime to the localized regime. This is confirmed in the 2D numerical simulations, since the averaged value of $\mathcal{F}_{12}$ over the maps gives 0.29 for $\lambda = 400$ nm (diffusion), 0.63 for $\lambda = 1000$ nm (intermediate regime), and 0.74 for $\lambda = 1500$ nm (localization). As a consequence, since both quantities $\mathcal{C}_{12}$ and $\mathcal{F}_{12}$ have a very different behavior in the diffusive and localized regimes, we expect $G^{(2)}$ to be quite a useful tool to discriminate between the two regimes.

To confirm this assertion we present maps of the classical and quantum second-order coherence functions evaluated in one realization of disorder for a 2D system in Fig. 3, for the diffusive regime with $\lambda = 400$ nm (top), the intermediate regime with $\lambda = 1000$ nm (middle), and the localized regime with $\lambda = 1500$ nm (bottom).

The maps for the classical second-order function $G^{(2)}_{\text{class}}$ (left panels) are very similar to the maps of the relative connectivity in Fig. 2: small values are obtained in the diffusive regime, while large clusters with high values of $G^{(2)}_{\text{class}}$ appear in the localization regime. In the quantum case, the maps of $G^{(2)}_{\text{quant}}$ (right panels) are slightly different, as a result of the influence of two factors: the relative connectivity $\mathcal{C}_{12}$ that governs the patterns close to the origin, corresponding to small distances between the two observation points, and the LDOS contrast $\mathcal{F}_{12}$ that acts as a background for larger separations. These differences can be traced back to the fact that the two second-order coherence functions include the factor $(1-\mathcal{F}_{12}^2)$, but differ by their dependence on the relative connectivity. In particular, while the variation of $G^{(2)}_{\text{class}}$ is directly proportional to $\mathcal{C}_{12}^2$, the quantum second-order coherence function, being proportional to $(1+\mathcal{C}_{12}^2)$, is less sensitive to $\mathcal{C}_{12}$. Moreover, for distant observation points such that $\mathcal{C}_{12} \simeq 0$, one has $G^{(2)}_{\text{class}} \to 1$, while $G^{(2)}_{\text{quant}} \to (1-\mathcal{F}_{12}^2)/2$, explaining why the background is affected by the spatial distribution of the LDOS in the case of single-photon sources.

The similarity between the spatial behavior of the classical coherence function $G^{(2)}_{\text{class}}$ and the mode connectivity suggests using the measurement of $G^{(2)}_{\text{class}}$ as a strategy to probe the appearance of localized modes in disordered media, and in particular the transition from diffusive transport to Anderson localization. The numerical study shows a robust signature of localization even in a single realization of disorder. As a supplemental analysis, disordered-averaged profiles of $G^{(2)}_{\text{class}}$ and $G^{(2)}_{\text{quant}}$ versus the distance $|\mathbf{r}_1-\mathbf{r}_2|$ between the observation points are presented in Appendix C.

V. CONCLUSION

In summary, we have introduced the concept of mode connectivity as a measure of the connection between two points at a given frequency. We have demonstrated the relevance of the connectivity in probing spatially localized modes in complex media. In the case of electromagnetic waves, we have defined observables that directly depend on the connectivity, and proposed schemes for practical implementations. The analysis could allow one to define an unambiguous approach to probe 3D Anderson localization of electromagnetic waves. It can be extended to other kinds of waves, and is relevant to all processes creating spatially localized modes.

ACKNOWLEDGMENTS

This work was supported by LABEX WIFI (Laboratory of Excellence within the French Program "Investments for the Future") under Grants No. ANR-10-LABX-24 and No. ANR-10-IDEX-0001-02 PSL*.

APPENDIX A: DERIVATION OF THE INEQUALITY BETWEEN CDOS AND LDOS

In this section we derive Eq. (2). We consider two monochromatic electric dipole sources (frequency ω) with dipole moments $\mathbf{p}_1 = p_1\mathbf{u}_1$ and $\mathbf{p}_2 = p_2\mathbf{u}_2$, located at positions $\mathbf{r}_1, \mathbf{r}_2$ in a linear and nonabsorbing medium. The electric field radiated at point $\mathbf{r}$ can be written in terms of the Green function

$$\mathbf{E}(\mathbf{r}) = \mu_0\omega^2\mathbf{G}(\mathbf{r},\mathbf{r}_1,\omega)\mathbf{p}_1 + \mu_0\omega^2\mathbf{G}(\mathbf{r},\mathbf{r}_2,\omega)\mathbf{p}_2. \tag{A1}$$

The total power emitted by the two sources outside the medium is

$$P = \frac{\varepsilon_0 c}{2}\int_S |\mathbf{E}\,|^2 dS, \tag{A2}$$

where S is a sphere with radius $R \to \infty$ that encloses the medium. Using Eq. (A1), this can be rewritten as

$$P = \frac{\pi\omega^2}{4\varepsilon_0}[|p_1|^2\rho_{11} + |p_2|^2\rho_{22} + 2\,\mathrm{Re}[p_1 p_2^*]\rho_{12}], \tag{A3}$$

where $\rho_{ij} = (2\omega/\pi c^2)\mathrm{Im}[\mathbf{u}_i\cdot\mathbf{G}(\mathbf{r}_i,\mathbf{r}_j,\omega)\cdot\mathbf{u}_j]$ is the CDOS for $i \neq j$ and the LDOS for $i = j$. Assuming that the two dipole sources are in-phase ($p_2 = \beta p_1$ with β a real number), we get

$$P = \frac{\pi\omega^2}{4\varepsilon_0}|p_1|^2[\rho_{22}\beta^2 + 2\rho_{12}\beta + \rho_{11}], \tag{A4}$$

which is a second-order polynom in β. As the radiated power P is positive, the determinant of this polynom must be negative, which yields

$$(\rho_{12})^2 \leqslant \rho_{11}\rho_{22}. \tag{A5}$$

This proves Eq. (2).

APPENDIX B: SECOND-ORDER COHERENCES

In this Appendix we recall the expression of the second-order coherence functions that were initially derived in Refs. [19] and [16] for classical and quantum sources, respectively.

1. Classical sources

We consider two incoherent classical sources located at positions $\mathbf{r}_1, \mathbf{r}_2$ in a linear and nonabsorbing medium, whose dipole moments $\mathbf{p}_1, \mathbf{p}_2$ are written as $\mathbf{p}_k(t) = p_k e^{\imath\phi_k(t)} e^{-\imath\omega t}\mathbf{u}_k$, where $\phi_1(t), \phi_2(t)$ are slowly varying uncorrelated random phases and $\mathbf{u}_1, \mathbf{u}_2$ are fixed orientations. Using Eqs. (A1) and (A2) above, the total power emitted outside the medium reads as

$$P = \frac{\pi\omega^2}{4\varepsilon_0}[|p_1|^2\rho_{11} + |p_2|^2\rho_{22} + 2\,\mathrm{Re}[p_1 p_2^* e^{\imath(\phi_1-\phi_2)}]\rho_{12}], \tag{B1}$$

where $\rho_{ij} = (2\omega/\pi c^2)\mathrm{Im}[\mathbf{u}_i \cdot \mathbf{G}(\mathbf{r}_i, \mathbf{r}_j, \omega) \cdot \mathbf{u}_j]$ is the CDOS for $i \neq j$ and the LDOS for $i = j$. When averaging over time, $e^{\imath(\phi_1-\phi_2)}$ vanishes in the interference term which leads to

$$\overline{P} = \frac{\pi\omega^2}{4\varepsilon_0}[|p_1|^2\rho_{11} + |p_2|^2\rho_{22}].$$

On the opposite, when looking at the variance of P, a cross product of interference terms survive the averaging process and

$$\overline{P^2} - (\overline{P})^2 = 2\left(\frac{\pi\omega^2}{4\varepsilon_0}\right)^2 |p_1 p_2|^2 (\rho_{12})^2,$$

which leads to the second-order coherence of the total emitted power

$$G^{(2)}_{\mathrm{class}} = \frac{\overline{P^2}}{(\overline{P})^2} = 1 + \frac{2|p_1 p_2|^2(\rho_{12})^2}{[|p_1|^2\rho_{11} + |p_2|^2\rho_{22}]^2}.$$

For emitters with the same amplitude ($|p_1| = |p_2|$), it simplifies to

$$G^{(2)}_{\mathrm{class}} = 1 + \tfrac{1}{2}\big[1 - \mathcal{F}_{12}^2\big]\mathcal{C}_{12}^2, \tag{B2}$$

where

$$\mathcal{F}_{12} = \frac{|\rho_{11} - \rho_{22}|}{\rho_{11} + \rho_{22}}, \quad \mathcal{C}_{12} = \frac{|\rho_{12}|}{\sqrt{\rho_{11}\rho_{22}}}$$

are the LDOS contrast and the mode connectivity between locations $\mathbf{r}_1$ and $\mathbf{r}_2$, respectively. Expression (B2) highlights that, for the coherence to reach high values ($G^{(2)}_{\mathrm{class}} \simeq 3/2$), the emitters must be located at positions that are well connected ($\mathcal{C}_{12} \simeq 1$) and where the LDOS is well balanced ($\mathcal{F}_{12} \simeq 0$).

2. Quantum sources

A similar derivation can be conducted for the case of quantum emitters, in which case the positive-frequency component of the electric-field operator can be connected to the source operators using the same Green tensors (see Ref. [16] for more details):

$$\mathbf{E}^{(+)}(\mathbf{r}) = \mu_0\omega^2\sigma_1^-\mathbf{G}(\mathbf{r}, \mathbf{r}_1)\mathbf{p}_1 + \mu_0\omega^2\sigma_2^-\mathbf{G}(\mathbf{r}, \mathbf{r}_2)\mathbf{p}_2.$$

Then the photodetection of one photon at position $\mathbf{r}_a$, with polarization state α_a along $\mathbf{e}_a$, is described by the operator $\mathbf{\Phi}_1(\mathbf{r}_a, \alpha_a) = E_a^\dagger E_a$, where $E_a = \mathbf{e}_a \cdot \mathbf{E}^{(+)}(\mathbf{r}_a)$. Similarly, one defines the photodetection of two photons at positions $(\mathbf{r}_a, \mathbf{r}_b)$, with respective polarizations (α_a, α_b), with the operator $\mathbf{\Phi}_2(\mathbf{r}_a, \alpha_a, \mathbf{r}_b, \alpha_b) = E_a^\dagger E_b^\dagger E_b E_a$. When integrating over all possible directions and polarizations one gets the operators

$$P_1 = \frac{\varepsilon_0 c}{2}\int_{S_a} d\mathbf{r}_a \sum_{\alpha_a} \mathbf{\Phi}_1(\mathbf{r}_a, \alpha_a),$$

$$P_2 = \left(\frac{\varepsilon_0 c}{2}\right)^2 \int_{S_a} d\mathbf{r}_a \int_{S_b} d\mathbf{r}_b \sum_{\alpha_a,\alpha_b} \mathbf{\Phi}_2(\mathbf{r}_a, \alpha_a, \mathbf{r}_b, \alpha_b),$$

where the prefactors are chosen to define observables corresponding to radiated power. Assuming the two emitters in the excited state, the probabilities to detect one or two photons over all output channels can then be simply expressed from the LDOS and CDOS at the positions of the emitters:

$$\langle P_1\rangle = \frac{\pi\omega^2}{4\varepsilon_0}(|p_1|^2\rho_{11} + |p_2|^2\rho_{22}),$$

$$\langle P_2\rangle = 2\left(\frac{\pi\omega^2}{4\varepsilon_0}\right)^2 |p_1 p_2|^2[\rho_{11}\rho_{22} + (\rho_{12})^2].$$

While the first quantity is similar to $\overline{P}$ for classical emitters, the second quantity differs as it does not contain terms with $(\rho_{ii})^2$, due to the fact that the sources are single-photon emitters. The second-order coherence for an emission integrated over directions and polarization is then

$$G^{(2)}_{\mathrm{quant}} = \frac{\langle P_2\rangle}{\langle P_1\rangle^2} = \frac{2|p_1 p_2|^2[\rho_{11}\rho_{22} + (\rho_{12})^2]}{[|p_1|^2\rho_{11} + |p_2|^2\rho_{22}]^2},$$

which for emitters with similar amplitudes simplifies to

$$G^{(2)}_{\mathrm{quant}} = \tfrac{1}{2}\big[1 - \mathcal{F}_{12}^2\big]\big[1 + \mathcal{C}_{12}^2\big]. \tag{B3}$$

Again, the later expression is quite useful as it readily shows that the second-order coherence reaches its maximum values ($G^{(2)}_{\mathrm{quant}} \simeq 1$) when $\mathcal{F}_{12} \simeq 0$ and $\mathcal{C}_{12} \simeq 1$.

APPENDIX C: ENSEMBLE-AVERAGED QUANTITIES

In order to overcome the dependence of the numerical results on a particular realization of the positions of the scatterers, we have repeated the process of generating the maps of the various observables over 240 realizations of the disordered medium. For an average over $X(\mathbf{r}_1, \mathbf{r}_2)$, we first compute an average over this ensemble for each position to produce a single averaged map. The points are then grouped by concentric rings to get a profile $\langle X\rangle(r)$ as a function of the distance $r = |\mathbf{r}_1 - \mathbf{r}_2|$ between the two positions. This enables

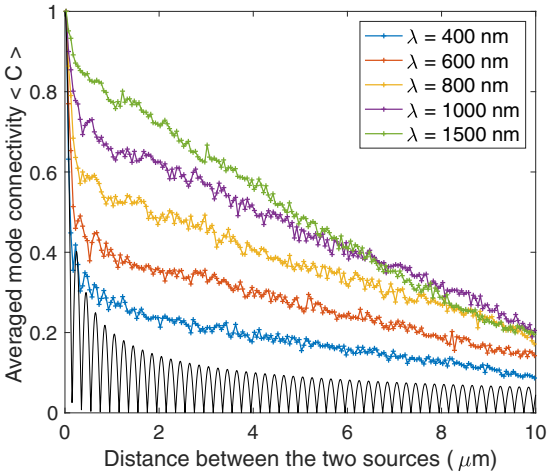

FIG. 4. Estimate of the averaged mode connectivity profile $\langle \mathcal{C}_{12} \rangle(r)$ over 240 realizations of disorder, as a function of the distance r between the two locations, for several values of the wavelength λ. The thin solid line at the bottom is $|J_0(k_0 r)|$ for $\lambda = 400$ nm, which recreates the connectivity of vacuum, for comparison of the behavior at small distances.

one to check that evaluations can rely in practice on a single realization of disorder, and to observe the qualitative evolution of an observable $X(\mathbf{r}_1, \mathbf{r}_2)$ when the system goes from the diffusive to the localized regime beyond the particular realization of disorder.

1. Mode connectivity

We first consider the mode connectivity $\mathcal{C}_{12}$ which is the absolute value of the CDOS between two positions normalized by their LDOSs and takes values between zero and 1. Maps of this quantity for a single realization of disorder are presented in the main text and show a qualitative change when going from the diffusive to the localized regime: in the diffusive regime $\mathcal{C}_{12}$ takes values clearly below one except close to the origin, while in the localized regime this quantity saturates for distances larger than the localization length ξ.

The averaged profile $\langle \mathcal{C}_{12} \rangle(r)$ is presented in Fig. 4.

In the diffusive regime, $\langle \mathcal{C}_{12} \rangle(r)$ quickly decreases with some oscillations, a reminder of the vacuum case where $\mathcal{C}_0(r) = |J_0(k_0 r)|$ for 2D TE modes. When the system enters the localization regime the drop becomes weaker as expected and high values are obtained up to several micrometers of distance.

2. Classical coherence

We apply the same treatment to the second-order coherence $G^{(2)}_{\text{class}}$ in the case of two classical emitters.

The averaged profile $\langle G^{(2)}_{\text{class}} \rangle(r)$ is presented in Fig. 5 and corroborates the observation made for a single realization of disorder: due to the large clusters of high values appearing in the localization regime, the profile increases with the wavelength. In the diffusive regime the averaged second-order coherence decreases strongly with small oscillations that are also present in the case of vacuum due to the varying mode connectivity.

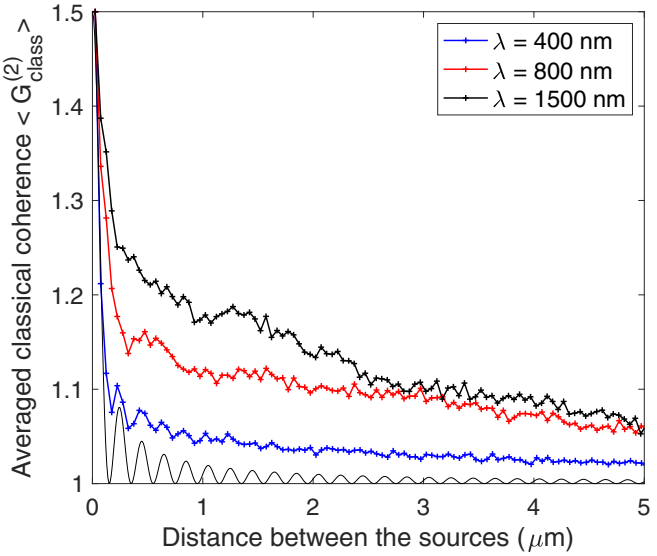

FIG. 5. Estimate of the averaged second-order coherence for classical sources $\langle G^{(2)}_{\text{class}} \rangle(r)$ as a function of the distance r between the two sources, for several values of the wavelength λ. The thin solid line at the bottom is $1 + |J_0(k_0 r)|^2/2$ for $\lambda = 400$ nm, which recreates the case of vacuum, for comparison of the behavior at small distances.

3. Quantum coherence

The same analysis can be conducted for the case of quantum emitters. The profile of the averaged second-order coherence $\langle G^{(2)}_{\text{quant}} \rangle(r)$ is presented in Fig. 6 as a function of the distance between the sources.

This time, while for small distances there is no clear difference in the averaged coherence $\langle G^{(2)}_{\text{quant}} \rangle$ between the diffusive and localized regimes, for large distances one has

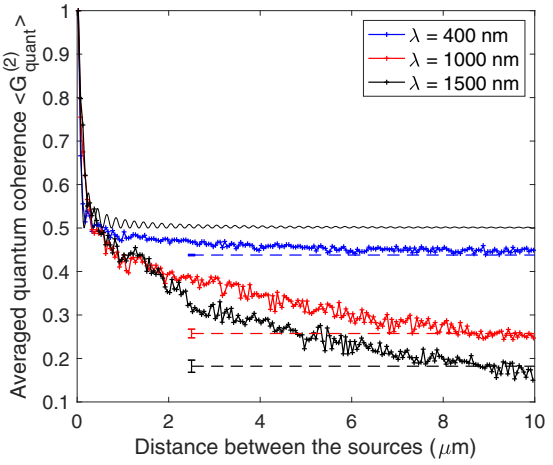

FIG. 6. Estimate of the averaged second-order coherence for quantum sources $\langle G^{(2)}_{\text{quant}} \rangle(r)$ as a function of the distance r between the two sources, for several values of the wavelength λ. Dashed lines represent estimates of the averaged value of $\langle (1 - \mathcal{F}_{12}^2)/2 \rangle$ and the error bars show the standard deviation when using one realization of disorder only. The thin solid line is $[1 + |J_0(k_0 r)|^2]/2$ for $\lambda = 400$ nm, which recreates the case of vacuum.

$\mathcal{C}_{12} \to 0$ and the second-order coherence heads towards $(1 - \mathcal{F}_{12}^2)/2$, which decreases from 0.5 for vacuum to lower values when the system goes from the diffusive to the localized regime. This asymptotic behavior is confirmed by numerical estimations of $\langle(1 - \mathcal{F}_{12}^2)/2\rangle$ presented in dashed horizontal lines of corresponding wavelengths.

[1] P. Sheng, *Introduction to Wave Scattering, Localization and Mesoscopic Phenomena* (Springer, New York, 2010).

[2] P. W. Anderson, Phys. Rev. **109**, 1492 (1958); Philos. Mag. B **52**, 505 (1985); S. John, Phys. Rev. Lett. **53**, 2169 (1984); A. Lagendijk, B. A. van Tiggelen, and D. S. Wiersma, Phys. Today **62**(8), 24 (2009).

[3] A. K. Sarychev and V. M. Shalaev, Phys. Rep. **335**, 275 (2000).

[4] E. Yablonovitch, Phys. Rev. Lett. **58**, 2059 (1987); S. John, *ibid.* **58**, 2486 (1987).

[5] W. L. Vos and L. A. Woldering, in *Light Localisation and Lasing: Random and Pseudorandom Photonic Structures*, edited by M. Ghulinyan and L. Pavesi (Cambridge University Press, Cambridge, UK, 2015).

[6] *Cavity Quantum Electrodynamics*, edited by P. Berman (Academic Press, New York, 1994); S. Haroche and J. M. Raimond, *Exploring the Quantum: Atoms, Cavities, and Photons* (Oxford University Press, Oxford, 2006).

[7] G. Anetsberger, O. Arcizet, Q. P. Unterreithmeier, R. Rivière, A. Schliesser, E. M. Weig, and T. J. Kippenberg, Nat. Phys. **5**, 909 (2009).

[8] M. Aspelmeyer, T. J. Kippenberg, and F. Marquardt, Rev. Mod. Phys. **86**, 1391 (2014).

[9] L. Sapienza, H. Thyrrestrup, S. Stobbe, P. D. Garcia, S. Smolka, and P. Lodahl, Science **327**, 1352 (2010); J. Gao, S. Combrie, B. Liang, P. Schmitteckert, G. Lehoucq, S. Xavier, X. Xu, K. Busch, D. L. Huffaker, A. De Rossi, and C. W. Wong, Sci. Rep. **3**, 1994 (2013).

[10] A. Cazé, R. Pierrat, and R. Carminati, Phys. Rev. Lett. **111**, 053901 (2013).

[11] J. B. Pendry, J. Phys. C **20**, 733 (1987); J. Bertolotti, S. Gottardo, D. S. Wiersma, M. Ghulinyan, and L. Pavesi, Phys. Rev. Lett. **94**, 113903 (2005); K. Y. Bliokh, Y. P. Bliokh, V. Freilikher, A. Z. Genack, B. Hu, and P. Sebbah, *ibid.* **97**, 243904 (2006).

[12] S. E. Skipetrov and I. M. Sokolov, Phys. Rev. Lett. **112**, 023905 (2014).

[13] A. Cazé, R. Pierrat, and R. Carminati, Phys. Rev. Lett. **110**, 063903 (2013).

[14] C. Sauvan, J. P. Hugonin, R. Carminati, and P. Lalanne, Phys. Rev. A **89**, 043825 (2014).

[15] R. Carminati, A. Cazé, D. Cao, F. Peragut, V. Krachmalnicoff, R. Pierrat, and Y. D. Wilde, Surf. Sci. Rep. **70**, 1 (2015).

[16] A. Canaguier-Durand and R. Carminati, Phys. Rev. A **93**, 033836 (2016).

[17] D. Laurent, O. Legrand, P. Sebbah, C. Vanneste, and F. Mortessagne, Phys. Rev. Lett. **99**, 253902 (2007).

[18] F. Riboli, P. Barthelemy, S. Vignolini, F. Intonti, A. De Rossi, S. Combrie, and D. S. Wiersma, Opt. Lett. **36**, 127 (2011).

[19] R. Carminati, G. Cwilich, L. S. Froufe-Pérez, and J. J. Sáenz, Phys. Rev. A **91**, 023807 (2015); **91**, 069903(E) (2015).